ADVANCES IN ATMOSPHERIC SCIENCES, VOL. 35, FEBRUARY 2018, 169–181

• **Original Paper** •

First Surface-based Estimation of the Aerosol Indirect Effect over a Site in Southeastern China

Jianjun LIU*[1] and Zhanqing LI[1,2]

[1]*Earth System Science Interdisciplinary Center, University of Maryland, College Park, MD* 20740*, USA*
[2]*State Laboratory of Earth Surface Process and Resource Ecology, College of Global Change and Earth System Science, Beijing Normal University, Beijing* 100875*, China*

(Received 24 April 2017; revised 15 August 2017; accepted 18 September 2017)

ABSTRACT

The deployment of the U.S. Atmospheric Radiation Measurement mobile facility in Shouxian from May to December 2008 amassed the most comprehensive set of measurements of atmospheric, surface, aerosol, and cloud variables in China. This deployment provided a unique opportunity to investigate the aerosol–cloud interactions, which are most challenging and, to date, have not been examined to any great degree in China. The relationship between cloud droplet effective radius (CER) and aerosol index (AI) is very weak in summer because the cloud droplet growth is least affected by the competition for water vapor. Mean cloud liquid water path (LWP) and cloud optical depth (COD) significantly increase with increasing AI in fall. The sensitivities of CER and LWP to aerosol loading increases are not significantly different under different air mass conditions. There is a significant correlation between the changes in hourly mean AI and the changes in hourly mean CER, LWP, and COD. The aerosol first indirect effect (FIE) is estimated in terms of relative changes in both CER (FIE_{CER}) and COD (FIE_{COD}) with changes in AI for different seasons and air masses. FIE_{COD} and FIE_{CER} are similar in magnitude and close to the typical FIE value of ~ 0.23, and do not change much between summer and fall or between the two different air mass conditions. Similar analyses were done using spaceborne Moderate Resolution Imaging Spectroradiometer data. The satellite-derived FIE is contrary to the FIE estimated from surface retrievals and may have large uncertainties due to some inherent limitations.

Key words: ground-based measurements, aerosol indirect effect, southeastern China

Citation: Liu, J. J., and Z. Q. Li, 2018: First surface-based estimation of the aerosol indirect effect over a site in southeastern China. *Adv. Atmos. Sci.*, **35**(2), 169–181, https://doi.org/10.1007/s00376-017-7106-2.

1. Introduction

Atmospheric aerosol particles can directly affect Earth's radiative balance by absorbing and scattering solar radiation (direct effects). They can also indirectly alter cloud microphysical and macrophysical properties, and precipitation, by serving as cloud condensation nuclei (CCN) (indirect effects). For a fixed cloud liquid water path (LWP), the cloud droplet size decreases with increasing CCN and reflects more energy to space. This is called the aerosol first indirect effect (FIE) or Twomey effect (Twomey, 1977). Under overcast sky conditions in the midlatitudes, the radiative forcing induced by the aerosol indirect effect varies from −3 to −10 W m^{-2} for each 0.05 increment in FIE (McComiskey and Feingold, 2008). Although the FIE has been studied extensively, it remains one of the largest uncertainties of all known climate forcing mechanisms (IPCC, 2013).

Using satellite measurements, the FIE has been investigated on regional (Nakajima et al., 2001; Liu et al., 2003; Menon et al., 2008; Yuan et al., 2008) and global (Bréon et al., 2002) scales. Such studies suffer from major inherent retrieval problems associated with retrievals of aerosol loading in general (Li et al., 2009), and aerosols near cloud edges in particular (Várnai and Marshak, 2014), which originate from the fundamental limitation that aerosol and cloud properties cannot be retrieved at the same time over the same location. These limitations can be overcome or lessened by ground and in-situ measurements (Feingold et al., 2003, 2006; Kim et al., 2003; Garrett et al., 2004; Pandithurai et al., 2009; Ma et al., 2010). McComiskey and Feingold (2012) argued that aerosol–cloud interactions (ACI) can only be assessed accurately from aircraft or ground-based in-situ data and depend on cloud and meteorological regimes (Wang et al., 2012; Zhang et al., 2016). Long-term observations of atmospheric variables and aerosol and cloud properties are thus needed to study the sensitivity of cloud properties to aerosols in different climatic regions.

* Corresponding author: Jianjun LIU
E-mail: jianjun5212@163.com

East Asia, especially southeastern China, is a fast developing and densely populated region where anthropogenic emissions of aerosol particles and precursors are high and the aerosol composition is complex (Li et al., 2007; Lee et al., 2010; Liu et al., 2011a, 2012). Aerosol optical properties over East Asia and their influence on the radiation budget at the surface (Xu et al., 2002; Xia et al., 2007; Liu et al., 2012) and within the atmosphere (Liu et al., 2012) have been investigated extensively. However, up until now, no FIE study has been done using ground-based measurements made in China due to the dearth of coincident aerosol, cloud, and meteorological observations (Liu et al., 2013, 2015). Only a few FIE studies using satellite measurements have been carried out (Yuan et al., 2008; Tang et al., 2014). Significant anti-Twomey effects have been reported based upon Moderate Resolution Imaging Spectroradiometer (MODIS) retrievals made over southeastern China (Yuan et al., 2008; Wang et al., 2014).

Two major international field experiments have been conducted in mainland China with the goal of studying aerosol properties and their direct and indirect effects: the "East Asian Study of Tropospheric Aerosols: An International Regional Experiment" (Li et al., 2007) and the "East Asian Study of Tropospheric Aerosols and Impact on Regional Climate" (Li et al., 2011). In the latter experiment, the Atmospheric Radiation Measurement (ARM) Mobile Facility (AMF-China) was deployed at Shouxian (SX), approximately 500 km northwest of Shanghai City, from May to December 2008. The experiment provided simultaneous observations of clouds, aerosols, radiative properties, and meteorological factors for the first time, and the opportunity to study the influence of aerosols on radiative fluxes, clouds, and precipitation in this key region.

Taking advantage of the extensive measurements made during AMF-China, the first comprehensive investigation into ACI over this polluted region is presented based upon the dataset compiled at SX. Brief descriptions of the measurements and methods used in the analyses are given in section 2. Section 3 presents the aerosol and cloud properties and analyses of the influence of aerosols on cloud properties for different seasons and air mass conditions. A summary is given in section 4.

2. Measurements and methodology

2.1. *Cloud optical and microphysical properties*

The cloud optical depth (COD) was retrieved following the method described by Marshak et al. (2004) and Chiu et al. (2010). The method is based on ground-based measurements of zenith radiances at red and near-infrared channels where the surface albedos in the two channels differ significantly. The downwelling zenith radiance was measured by a two-channel narrow field-of-view (NFOV) radiometer with a 5.7° field of view at 673 and 870 nm and at a 1-s time resolution. Biases in the NFOV radiance measurements were quantified through comparisons with Aerosol Robotic Network sun photometer radiance measurements, which are deemed to be more accurate (Holben et al., 1998). In general, the two datasets correlate well at both wavelengths. However, NFOV-measured zenith radiances at 673 nm are underestimated by ~ 11%. On the basis of regression analyses, adjusted NFOV zenith radiances at 673 nm, $F_{673,\mathrm{adj}}$, were calculated using the following formula:

$$F_{673,\mathrm{adj}} = 1.1066 F_{673,\mathrm{obs}} - 0.0007 \,, \tag{1}$$

where $F_{673,\mathrm{obs}}$ represents the originally-measured zenith radiances. The total uncertainty in COD retrievals using the zenith radiance measurement method is ~ 17% (Chiu et al., 2010).

Atmospheric brightness temperatures at 12 frequencies were measured by a profiling microwave radiometer (TP/WVP-3000, Radiometrics Corporation, US) and installed at SX. Vertical profiles of temperature and humidity, as well as integrated water vapor column amount and LWP, were retrieved with a 1-min time resolution using this instrument. Retrieval coefficients were derived for each season to account for seasonal variations in the atmosphere and in the mean radiating temperature. Typical uncertainties in LWP retrievals from microwave radiometers are ~ 20 g m^{-2} for LWP < 200 g m^{-2} and ~ 10% for LWP > 200 g m^{-2} (Liljegren et al., 2001; Liljegren and Lesht, 2004; Dong et al., 2008). When COD and LWP are retrieved, the cloud droplet effective radius (CER) can be calculated using the following equation:

$$\tau = \frac{3\mathrm{LWP}}{2\rho_{\mathrm{w}} r_{\mathrm{e}}} \,, \tag{2}$$

where τ represents COD, r_{e} represents CER, and ρ_{w} is the density of water. The uncertainty in CER is determined by the uncertainties in COD and LWP. Cloud retrievals following the same method have been used to assess ACI in marine stratus clouds (McComiskey et al., 2009). Cloud-base heights were measured by a micropulse lidar (MPL), which is an elastic backscatter lidar developed by the NASA Goddard Space Corporation (Wang and Sassen, 2001). The MPL installed at SX operates at 527 nm and has a 30-m range vertical resolution and a 30-s time resolution.

In this study, clouds with base heights greater than 3 km and CER > 25 μm or CER < 2 μm are excluded because these are unrealistic values for low-level warm clouds (Bulgin et al., 2008). Also, clouds with LWP < 20 g m^{-2} and LWP > 700 g m^{-2} are excluded to remove unaccounted-for biases and rainy periods, respectively (Min et al., 2003; Liu et al., 2013). To examine the influence of aerosols on non-precipitating cloud properties, only clouds with LWP < 300 g m^{-2} are analyzed (Chiu et al., 2012; Harikishan et al., 2016).

2.2. *Aerosol properties*

Total scattering coefficients (σ) of aerosol particles with diameters < 1 μm and < 10 μm were measured by two three-wavelength (450, 550, and 700 nm) nephelometers (Model 3653, TSI, US) with a 1-min time resolution under dry conditions with relative humidity (RH) less than 40% and varying

RH levels. The nephelometers were calibrated weekly using CO_2 gas to ensure the accuracy of measurements. The uncertainty in nephelometer-measured σ ranges from 1–4 Mm^{-1} for 1-min averages (Heintzenberg et al., 2006). Here, the σ of particles with diameters < 10 μm measured at 450 and 550 nm under dry conditions were used to calculate the Ångström exponent (AE). The aerosol index (AI) was then calculated using the σ at 550 nm and the AE. The AI was used as a proxy for CCN to study ACI because AI is more related to CCN concentration than σ (Nakajima et al., 2001; Liu and Li, 2014). The aerosol properties were then matched with cloud retrievals and integrated over 1-min time intervals.

2.3. *Air mass trajectory classification*

The prevalent meteorological conditions and dominant aerosol type largely depend on the air mass. Potential differences in aerosols, cloud properties, and ACI for different air masses at SX were accounted for using a Hybrid Single-Particle Lagrangian Integrated Trajectory model simulation (Stein et al., 2015; Rolph, 2016). All three-day simulated air mass back trajectories arriving at the site at 500 m were classified into four major clusters: air masses originating from the northwest (cluster I), the northeast (cluster II), the East China Sea (cluster III), and the south (cluster IV) of China. Detailed descriptions of each air mass are discussed in the study by Liu et al. (2011b). The number of days with a cluster I, II, III, and IV air mass is 30, 46, 81, and 37, respectively. This corresponds to 15.5%, 23.7%, 41.8%, and 19%, respectively, of the total number of days of the field campaign at SX.

3. Results

3.1. *Characteristics of aerosol and cloud properties during the observation period*

3.1.1. *Seasonal characteristics of aerosol and cloud properties*

Mean aerosol and cloud properties in summer (June, July, and August; JJA), fall (September, October, and November; SON), and winter (December; Dec.) are summarized in Table 1. The probability distribution functions (PDFs) of aerosol properties (σ, AE, and AI) and cloud properties (COD, LWP, and CER) for JJA, SON, and Dec. are shown in Fig. 1. The number of aerosol and cloud samples in each season are shown in panels (c) and (f), respectively, of the figure. Aerosol loadings in JJA and Dec. are similar and smaller than that in fall. The small magnitude of mean σ in JJA occurs because there is more frequent precipitation and relatively higher mixing heights in that season. Relatively strong winds play a major role in the low mean σ in Dec. (Fan et al., 2010). Mean values of AE in JJA, SON, and Dec. are similar, suggesting that aerosols have similar mean aerosol particle sizes during the three periods. The broad distribution of AE (Fig. 1b) indicates that aerosol particle sizes in all seasons are highly variable.

The COD varies greatly, with larger mean values in Dec. than in JJA and SON (Fig. 1d). Distributions of COD in JJA and SON have similar shapes and significantly more cloud samples with large COD are observed in Dec. Clouds have the largest LWP values in SON and similar values in JJA and Dec. (Fig. 1e). During all three periods, clouds have similar distributions of LWP, with more samples in the range of 60–120 g m^{-2}. The CER is smallest in Dec., with most of the distribution located below 5 μm (Fig. 1f).

3.1.2. *Characteristics of aerosol and cloud properties under different air mass conditions*

Table 1 also lists the means and standard deviations of aerosol and cloud properties for each air mass type. Air masses I and IV have the highest and smallest mean values of σ, respectively. The σ for air mass IV has a narrower distribution than that for other air masses (Fig. 2a). Figure 2b shows that relatively more aerosol particles with large particle sizes arrive at the site from the northwest and northeast, and relatively more aerosol particles with small particle sizes arrive at the site from the east and southeast. The AIs for the different air masses have similar properties to the σ.

Mean values of COD and LWP are largest (smallest) when air mass I (IV) influences the site, and the mean CER is largest (smallest) under air mass IV (I) conditions. Figure 2e shows that most of the LWP values are less than 200 g m^{-2} for all air masses. The PDFs of CER for each air mass in Fig. 2f have similar shapes. A shift in CER toward larger values

Table 1. Means and standard deviations of aerosol, cloud, and surface meteorological variables in summer (JJA), fall (SON), and December (Dec.) and for each air mass type.

	σ (Mm^{-1})	AE	AI	COD	LWP (g m^{-2})	CER (μm)
JJA	222 ± 156	1.24 ± 0.33	241 ± 148	29.4 ± 22.2	160 ± 115	9.8 ± 5.0
SON	445 ± 343	1.26 ± 0.25	542 ± 411	39.5 ± 23.9	185 ± 131	7.5 ± 3.7
Dec.	281 ± 172	1.28 ± 0.28	355 ± 212	60.8 ± 22.2	155 ± 92	3.7 ± 1.6
I	562 ± 318	1.15 ± 0.23	600 ± 306	62.9 ± 24.8	281 ± 194	6.4 ± 3.4
II	425 ± 313	1.18 ± 0.25	490 ± 347	42.3 ± 24.2	169 ± 150	6.2 ± 4.2
III	295 ± 272	1.29 ± 0.31	361 ± 353	40.3 ± 25.8	185 ± 119	8.0 ± 4.1
IV	232 ± 142	1.26 ± 0.30	247 ± 137	25.3 ± 19.8	147 ± 91	11.0 ± 5.1

σ: Aerosol scattering coefficients at 550 nm under dry conditions with particle diameters less than 10 μm; COD: Cloud optical depth; LWP: Liquid water path; CER: Cloud droplet effective radius; JJA: June, July, and August; SON: September, October, and November; Dec.: December.

I–IV: Air masses originating from the northwest (cluster I), the northeast (cluster II), the East China Sea (cluster III), and the south (cluster IV) of the site.

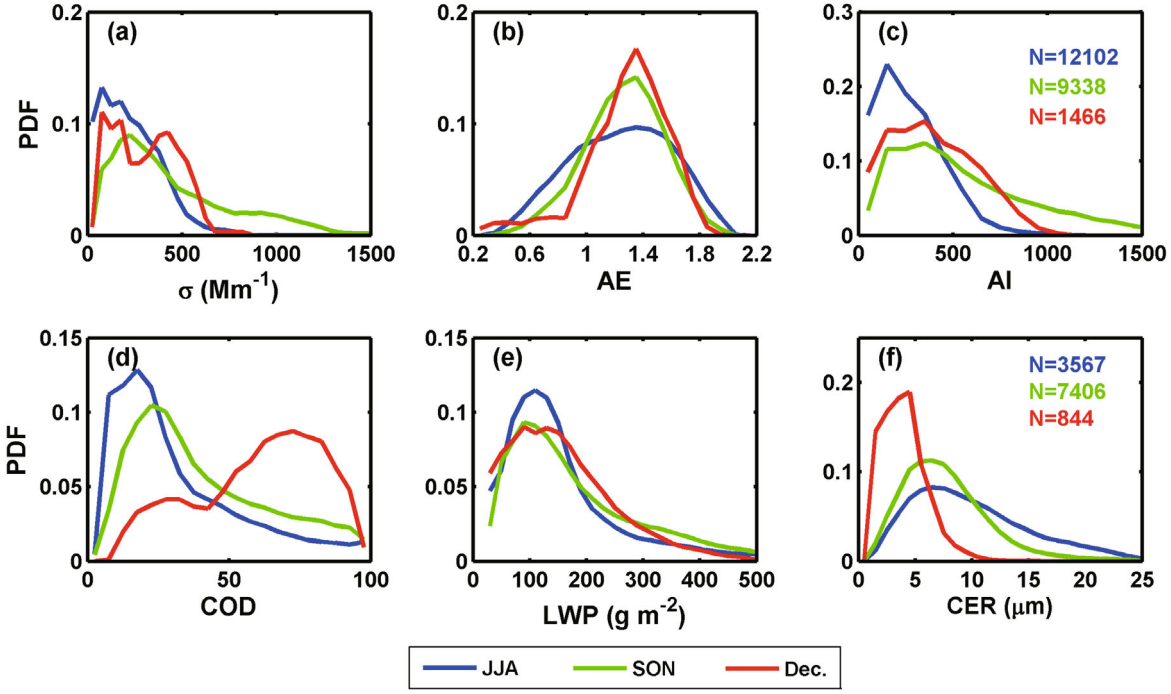

Fig. 1. PDFs of aerosol and cloud properties in JJA (blue lines), SON (green lines) and December (red lines): (a) scattering coefficient (σ); (b) Ångström exponent (AE), (c) aerosol index (AI); (d) cloud optical depth (COD), (e) liquid water path (LWP); and (f) cloud droplet effective radius (CER). The number of aerosol and cloud samples in each season are shown in panels (c) and (f), respectively.

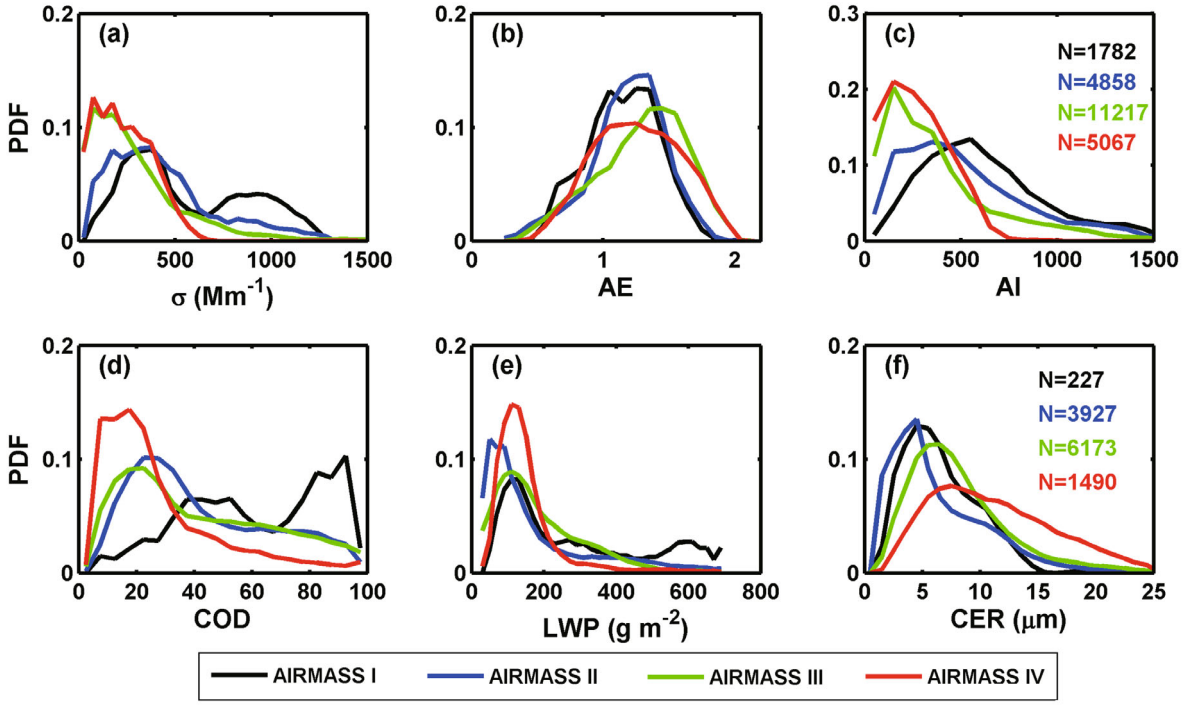

Fig. 2. As in Fig. 1 but for different air masses.

from air mass I to air mass IV is apparent.

3.1.3. *Diurnal cycle of aerosol and cloud properties*

Hourly mean aerosol and cloud properties are calculated from all available samples in each hour from 0800 to 1600 local standard time (LST; Fig. 3). Hourly mean σ varies significantly, with the highest value in the morning and the lowest value in the afternoon. The high value of σ in the morning is mainly due to local cooking emissions and emissions from transportation sources, as well as the low mixing height because of the low temperature (Fan et al., 2010; Liu et al., 2011b). After sunrise, the temperature, and thus the mix-

ing height, increases, which leads to the dilution of surface aerosols with air aloft and results in a corresponding decrease in σ (Fan et al., 2010). Figure 3b shows that AE slightly increases from morning to afternoon, but the increase is small, suggesting that the aerosol particle size does not change much from morning to afternoon. The diurnal cycle of AI in Fig. 3c is similar to the diurnal cycle of σ.

The hourly mean COD is nearly constant from morning to noon, and then significantly increases from noon to late afternoon, suggesting that clouds attenuate more in the afternoon than in the morning. In general, the variations in hourly mean LWP from morning to afternoon seen in Fig. 3e vary in the same way as the hourly mean COD, with maxima occurring around noon. CER increases slightly from morning to noon, then decreases significantly (Fig. 3f).

3.2. *Influence of aerosols on cloud properties*

3.2.1. *Relationship between cloud properties and AI for different seasons*

Figures 4a–c show the logarithmic relationship between CER, LWP, COD, and AI during the JJA and SON periods, respectively. The total number of samples in JJA and SON is 2343 and 2812, respectively. Cloud properties were sorted as a function of AI and averaged in each of the 10 AI bins. Each bin contains the same number of samples. Major meteorological parameters (e.g., RH), as well as large-scale dynamic (e.g., vertical velocity) and thermodynamic (e.g., lower-tropospheric stability) parameters, show no sig-

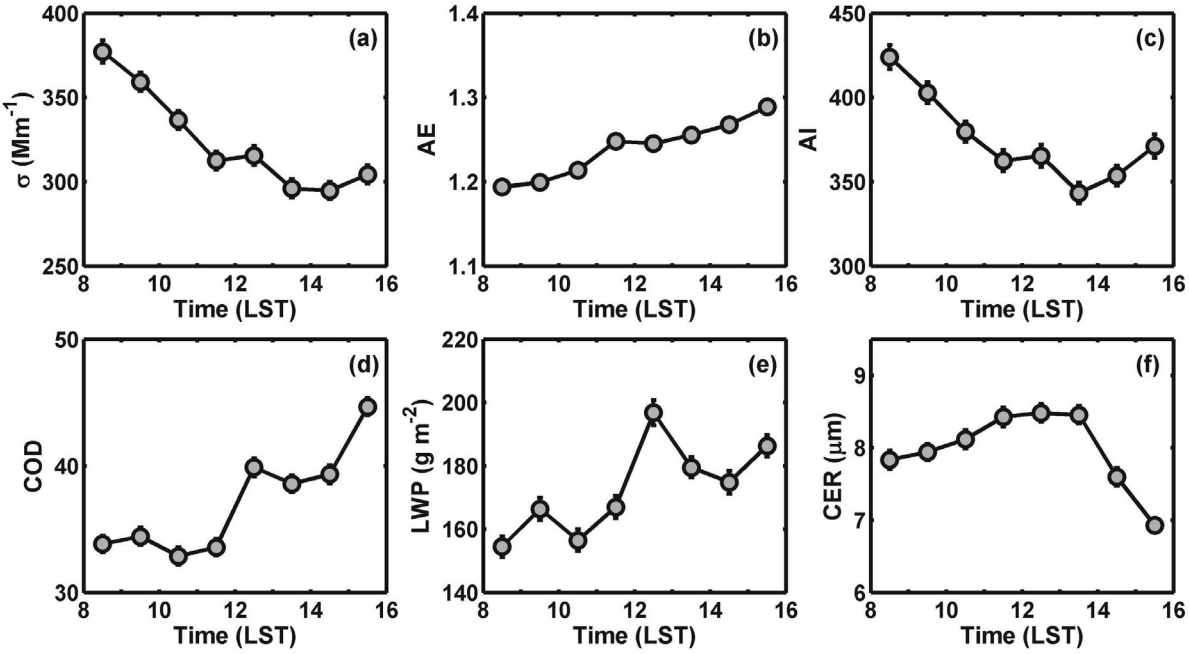

Fig. 3. Diurnal cycle of the (a) σ, (b) AE, (c) AI, (d) COD, (e) LWP, and (f) CER during the observation period.

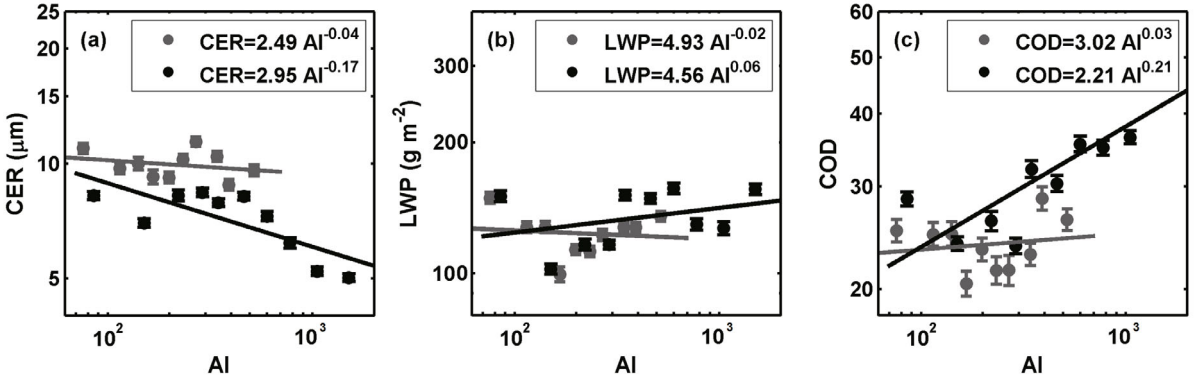

Fig. 4. The (a) CER, (b) LWP and (c) COD as a function of AI in summer (gray) and fall (black). Cloud properties were first sorted as a function of AI and averaged in each of the 10 AI bins. Error bars represent the confidence level of the mean values if independent data are assumed, and are calculated as $sd^2/\sqrt{N-2}$, where sd^2 is the standard deviation of the cloud property data in a bin and N is the number of data points in the AI bin. Axes are scaled logarithmically.

nificant seasonal differences when going from low AI to high AI. For both JJA and SON, CER decreases as AI increases, but the relationship between CER and AI is very weak for JJA. As AI increases from the lowest quartile to the highest quartile, CER decreases by ~ 9% (from 10.3 μm to 9.4 μm) in JJA and by ~ 36% (from 7.8 μm to 5.0 μm) in SON. The strength of the aerosol impact on CER is quantified by the linear regression slope of the CER–AI relationship in log–log scale (Costantino and Bréon, 2013). The powers of the calculated exponential regression functions are equal to −0.04 and −0.17 in JJA and SON, respectively. Based on MODIS measurements, Yuan et al. (2008) showed that the slope of the correlation between CER and aerosol optical depth (AOD) is driven primarily by the water vapor amount, which explains 70% of the variance. The slope of the correlation between CER and AOD is positive for moist regions and negative for dry regions (Yuan et al., 2008). The higher water vapor amount in JJA than in SON may thus partly explain the weaker CER sensitivity to aerosol loading in JJA, in addition to other potential factors (e.g., dynamic and thermodynamic conditions, and aerosol type).

Figure 4b shows that, in JJA, LWP does not strongly depend on AI. As AI increases from the lowest quartile to the highest quartile, the mean value of LWP changes from 136 g m^{-2} to 130 g m^{-2}, which is a decrease of ~ 4%. The linear regression slope of the LWP–AI relationship in log–log scale is −0.02. During the SON period, the mean LWP increases by ~ 10% (from 126 g m^{-2} to 139 g m^{-2}) as AI changes from the lowest quartile to the highest quartile. The linear regression slope in log–log scale is 0.06. Results from current studies on the response of LWP to increases in aerosol loading are diverse, showing a positive correlation in some studies (Quaas et al., 2009; Wang et al., 2013) and a negative correlation in others (Twohy et al., 2005; Lee et al., 2009). The balance between two competitive processes determines the response of LWP to increases in aerosol loading: (1) moistening from precipitation suppression; and (2) drying from the increased entrainment of dry overlaying air. Since the two processes commonly occur together, the difference in the response of LWP to increases in AI between the two seasons possibly happens because the different meteorology, aerosols, and other settings in each season may make one process dominate over the other.

During the JJA period, COD increases with increasing AI, but not in a significant way. As AI changes from the lowest quartile to the highest quartile, the mean COD increases by ~ 7% (from 24.9 to 26.6). The weak changes in LWP and CER with increasing AI lead to a weak response of COD to AI. Figure 4c shows that, during the SON period, COD significantly increases with increasing AI. The mean value of COD increases by ~ 63% (from 26.3 to 43.0) as AI increases from the lowest quartile to the highest quartile. The slope of the COD–AI exponential regression line is 0.21. This large value suggests that aerosols favor the growth of clouds in terms of thickness by inhibiting CER (Twomey, 1977; Liu et al., 2016), and thus enhance the reflection of solar radiation by clouds.

3.2.2. *Relationship between cloud properties and AI under different air mass conditions*

Figures 5a–c show the logarithmic relationships between CER, LWP, COD and AI under different air mass conditions. Due to the limited number of aerosol and cloud samples for air masses I and IV, only samples under air mass II and III conditions are analyzed. Major meteorological parameters under both air mass conditions show no significant difference as AI increases. Under both air mass conditions, CER significantly decreases as AI increases, suggesting a strong influence of aerosols on cloud microphysical properties. The mean CER decreases by ~ 34% (from 5.8 to 3.8 μm) and by ~ 22% (from 8.1 to 6.3 μm) under air mass II and III conditions, respectively. No significant difference in the strength of the sensitivity of CER to increasing aerosols is seen between both air mass types.

Figure 5b shows that, under both air mass II and III conditions, LWP increases with increasing AI, but not in a significant way. As AI increases from the lowest quartile to the highest quartile, the mean LWP increases by 20% (from 94 to 113 g m^{-2}) and by 12% (from 135 to 151 g m^{-2}) under air mass II and III conditions, respectively. The strength of the LWP sensitivity to increasing aerosols is almost the same under air mass II and III conditions.

Figure 5c shows that, as AI increases, the mean COD increases by ~ 26% (from 34 to 43) and by ~ 25% (from 32

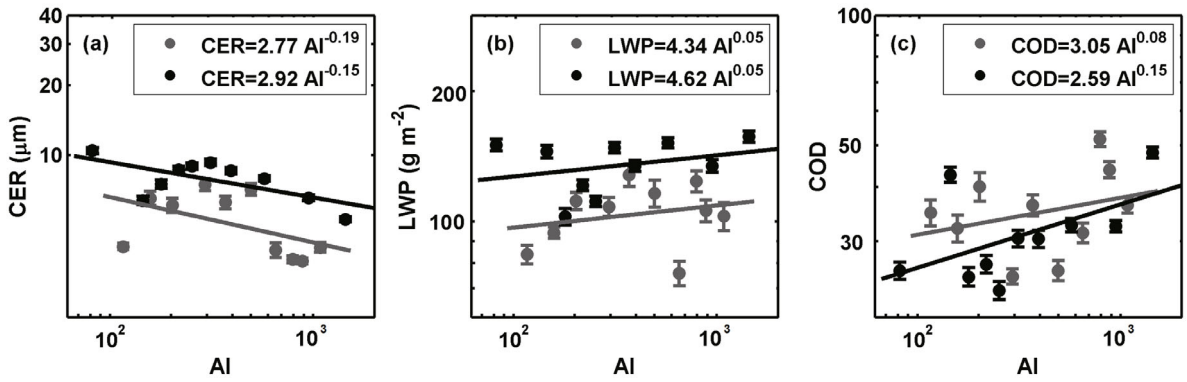

Fig. 5. As in Fig. 4 but for air mass II (gray) and air mass III (black).

to 40) when air mass II and III, respectively, influence the site. The slope of the COD–AI exponential regression line is larger for samples influenced by air mass II (0.15) than for those influenced by air mass III (0.08), suggesting that under air mass II conditions, the sensitivity of COD to aerosols is greater.

3.3. *Potential role played by aerosols in the evolution of cloud properties*

Figure 6 shows the PDFs of percentage changes in hourly mean CER (ΔCER), LWP (ΔLWP), and COD (ΔCOD) for the lowest (ΔAI_L) and highest (ΔAI_H) quartile of percentage changes in AI. The percentage change in hourly mean cloud and aerosol properties is calculated as:

$$\Delta M = (\overline{M}_i - \overline{M}_{i-1})/\overline{M}_{i-1}, i = 9, \ldots, 15 \quad (3)$$

where M represents an aerosol or cloud variable, ΔM is the percentage change in the variable, $\overline{M}$ is the mean value over an hour of the variable, and i is the LST. When $i = 9$, $\overline{M}_{i-1}$ represents the mean value of the variable from 0800 LST to 0900 LST, and $\overline{M}_i$ represents the mean value of the variable from 0900 LST to 1000 LST. Due to the relatively short time scale (one hour), such a procedure can be viewed as a high temporal filter, since it largely removes the effects of synoptic and large-scale processes. The mean values of ΔAI_L and ΔAI_H are −0.26 and 0.22, respectively, which represents a decrease by 26% and an increase by 22%, respectively. The PDF of ΔCER in Fig. 6a shows that there is a shift in ΔCER toward positive values for the ΔAI_L case and toward negative values for the ΔAI_H case. For the ΔAI_L case, the mean ΔCER is 0.18 (an increase of 18%), and for the ΔAI_H case the mean ΔCER is −0.06 (a decrease of 6%). A negative relationship between ΔCER and ΔAI is found, which suggests that when AI increases after an hour, the CER tends to decrease simultaneously. Figures 6b and c show that ΔLWP and ΔCOD are positively correlated with ΔAI. For the ΔAI_L case, there are more samples with ΔLWP < 0 and ΔCOD < 0 than with ΔLWP > 0 and ΔCOD > 0, but for the ΔAI_H case the opposite is seen. This suggests that, when AI increases after an hour, the LWP and COD tend to increase simultaneously. In general, the larger the ΔAI, the smaller the ΔCER and the larger the ΔLWP and ΔCOD.

3.4. *Aerosol FIE*

The aerosol FIE can be calculated as

$$\mathrm{FIE} = \left.\frac{\partial \ln \mathrm{COD}}{\partial \ln \alpha}\right|_{\mathrm{LWP}} = -\left.\frac{\partial \ln \mathrm{CER}}{\partial \ln \alpha}\right|_{\mathrm{LWP}}, \quad (4)$$

where α is the CCN concentration or a CCN proxy, such as aerosol number concentration, AOD, etc. In the current study, aerosol and cloud measurements were first separated into different LWP bins ranging from 20 to 300 g m^{-2} in 20 g m^{-2} increments. Then, the FIE in each LWP bin was estimated using the linear regression slope of all scatter points representing the CER/COD and AI relationship in log–log scale. The FIE estimated from changes in CER and COD with changes in AI is expressed as $\mathrm{FIE_{CER}}$ and $\mathrm{FIE_{COD}}$, respectively.

Figure 7 shows the magnitude of $\mathrm{FIE_{CER}}$ in each LWP bin for the different seasons (Figs. 7a and b for JJA and SON, respectively) and for different air mass conditions (Figs. 7c and d for air mass II and air mass III, respectively). Only cases with sample numbers greater than 50 and with a calculated $\mathrm{FIE_{CER}}$ that is statistically significant at the 95% confidence level are considered. The mean value of $\mathrm{FIE_{CER}}$ is 0.16 ± 0.06 and 0.17 ± 0.06 in JJA and SON, respectively, which suggests that $\mathrm{FIE_{CER}}$ has no systematically strong seasonal variation at the SX site. The mean $\mathrm{FIE_{CER}}$ values under air mass II and III conditions (0.23 ± 0.09 and 0.20 ± 0.06, respectively) are not significantly different. The $\mathrm{FIE_{CER}}$ in JJA and when air mass II is over the site increases as LWP increases. In SON and when air mass III is over the site, the $\mathrm{FIE_{CER}}$ increases and then slightly decreases as LWP increases. Figure 8 shows the magnitude of $\mathrm{FIE_{COD}}$ for each season (Fig. 8a for JJA and Fig. 8b for SON) and for each air mass (Fig. 8c for air mass II and Fig. 8d for air mass III). The $\mathrm{FIE_{COD}}$ is similar to the $\mathrm{FIE_{CER}}$ in each season and under each air mass condition. The variation in $\mathrm{FIE_{COD}}$ with increasing LWP is also consistent with that of $\mathrm{FIE_{CER}}$ in each season and under each air mass condition.

It is difficult to directly compare various estimates of FIE from different studies because the conditions under which FIE is calculated, e.g., LWP ranges and the CCN proxy used,

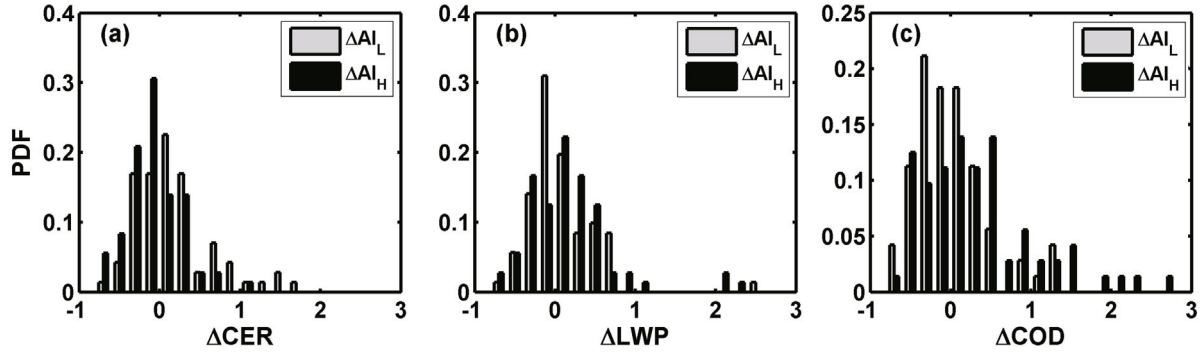

Fig. 6. PDFs of percentage changes in the hourly means of (a) CER (ΔCER), (b) LWP (ΔLWP), and (c) COD (ΔCOD) for the lowest (ΔAI_L, in gray) and highest (ΔAI_H, in black) quartile of changes in AI.

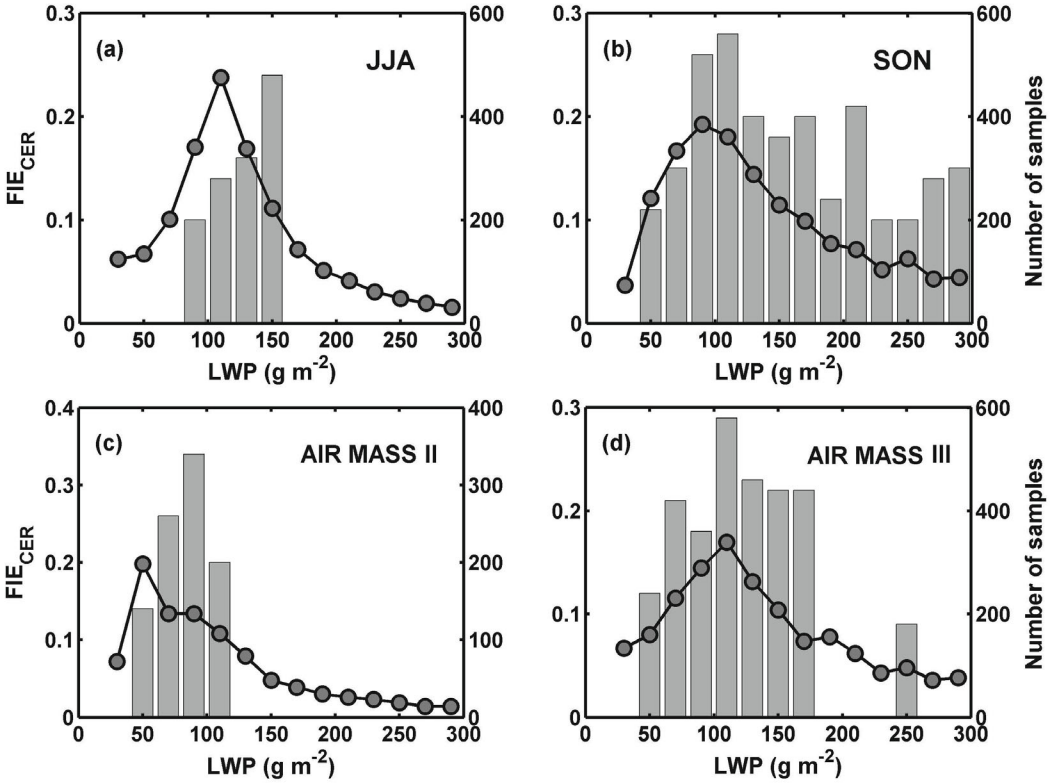

Fig. 7. Magnitudes of the first indirect effect (FIE) (bars) estimated from changes in CER with changes in AI (FIE_{CER}) in each LWP bin from 20 to 300 g m^{-2} in 20 g m^{-2} intervals in (a) JJA and (b) SON, and (c) under air mass II and (d) air mass III conditions. The dotted lines indicate the number of samples in each LWP bin (right-hand ordinates). Only cases with sample numbers greater than 50 and with a calculated FIE_{CER} that is statistically significant at the 95% confidence level are considered.

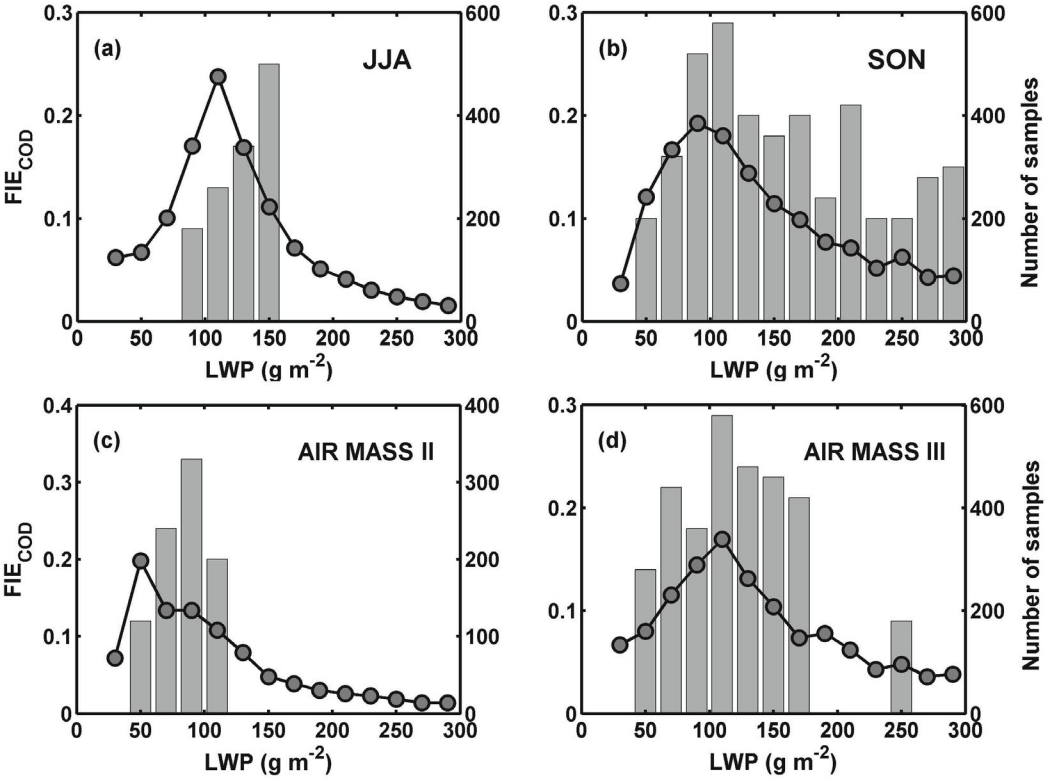

Fig. 8. As in Fig. 7 but for the magnitude of the FIE estimated from changes in COD with changes in AI (FIE_{COD}).

and the method used to retrieve CER, to which the FIE might be sensitive (Rosenfeld and Feingold, 2003; Feingold et al., 2006; McComiskey et al., 2009; Zhao et al., 2012), are usually different. Most studies have shown that the magnitude of the FIE generally lies between 0.02 and 0.33, with most values between 0.05 and 0.25 (Zhao et al., 2012). Ground-based studies that focus on FIE and its quantification over East Asia, especially over China, are few due to the lack of simultaneous observations of aerosol and cloud properties, with the latter being the primary constraint. The FIE metric estimated from satellite measurements ranges from 0.02 to 0.20 for midlatitude continental clouds (Nakajima et al., 2001; Myhre et al., 2007) and is usually lower than that estimated in airborne- and surface-based studies. Table 2 summarizes results from previous studies on estimating FIE for non-precipitating, warm clouds based on ground measurements. The FIE metric calculated in this study generally falls within the range of the published values listed in Table 2, and is close to the typical FIE value of ~ 0.23 reported by Twomey (1977).

3.5. *FIE calculated from MODIS measurements*

Based on MODIS measurements of AOD and cloud microphysical properties, previous studies have demonstrated a positive relationship between cloud CER and AOD over southeastern China (Yuan et al., 2008; Tang et al., 2014). However, a significant decrease in CER with increased surface-measured aerosol loading is found in this study. Ten years (2003–2012) of MODIS/Terra and MODIS/Aqua retrievals of AOD and cloud microphysical properties made over the site were used to examine the relationship between AOD and CER, and to see whether there are any discrepancies with results derived from surface measurements. Aerosol and cloud properties were averaged over a 50 km ×50 km box centered on the SX site. To ensure data quality, the following criteria were used (Yuan et al., 2008): (1) only overcast cloudy pixels flagged as "high confidence" by the retrieval algorithm were selected; (2) clouds with COD < 5 were discarded to reduce the uncertainty in cloud particle size retrievals; and (3) only liquid water clouds with CER < 25 μm were chosen. Figure 9 shows MODIS-retrieved CER as a function of MODIS-retrieved AOD for different LWP bins. Only samples from LWP bins with more than 50 samples were used to estimate the FIE. During the JJA period, the relationship between CER and AOD is very weak, with the slope fluctuating around zero across all LWP bins. During the SON period, a positive correlation between CER and AOD is found, especially in the LWP range of 20 to 40 g m^{-2}. The weak and positive correlation between CER and AOD at the site is consistent with previous MODIS studies (Yuan et al., 2008; Tang et al., 2014), but contrary to the results obtained from surface-based retrievals presented in the current study. Substantially smaller droplet sizes under high CCN concentration conditions were simulated at the SX site using the Weather Research and Forecasting model (Fan et al., 2012), which is consistent with the results of this study.

Results show that the effect of aerosols on cloud microphysical properties retrieved from satellite measurements are weaker, even contrary to the Twomey effect, and are affected by much more noise, compared with the results from surface-based measurements. One reason is that a passive remote sensing instrument like MODIS cannot measure aerosol and cloud properties simultaneously because clouds block signals from aerosols located beneath them. This introduces some uncertainties when analyzing the relationship between aerosol and cloud microphysical properties. A second reason is that satellite-retrieved CER typically represents the cloud particle size near the top of optically thick clouds, while surface-retrieved CER, weighted by the water mass in the cloud, represents the layer mean particle size. Under the same aerosol loading conditions, the MODIS-derived CER is significantly larger than the CER estimated from surface measurements (figure not shown), which possibly masks the influence of aerosols on cloud properties. In addition, since most aerosol particles are found within the boundary layer over this region (Liu et al., 2012), the CER derived from sur-

Table 2. FIE estimates based on ground-based measurements from different studies.

Site	CCN/CCN proxy	FIE	Reference
Rural continental site at Mahabubnagar, India	CCN	0.01–0.23 with a mean value of 0.14 ± 0.09	Harikishan et al. (2016)
Graciosa Island, Azores	Aerosol number concentration	0.06–0.10 with a mean value of 0.07 ± 0.01	Liu et al. (2016)
Cape Hedo, Japan	Aerosol scattering coefficient	0.04–0.13 with a mean value of 0.07 ± 0.04	Pandithurai et al. (2009)
Pt. Reyes, California, U.S.	CCN; Aerosol scattering coefficient; Aerosol index	0.10–0.14; 0.04–0.14; 0.07–0.15	McComiskey et al. (2009)
Southern Great Plains site, U.S.	Aerosol scattering coefficient	0.04–0.17 with a mean value of 0.10 ± 0.05	Kim et al. (2008)
Southern Great Plains site, U.S.	Aerosol extinction	0.14–0.26	Feingold et al. (2006)
North Slope of Alaska, U.S.	Aerosol scattering coefficient	0.11–0.19	Garrett et al. (2004)
Southern Great Plains site, U.S.	Aerosol extinction	0.02–0.16 with a mean value of 0.10 ± 0.05	Feingold et al. (2003)
Southern Great Plains site, U.S.	Aerosol scattering coefficient	0.12–0.14	Kim et al. (2003)

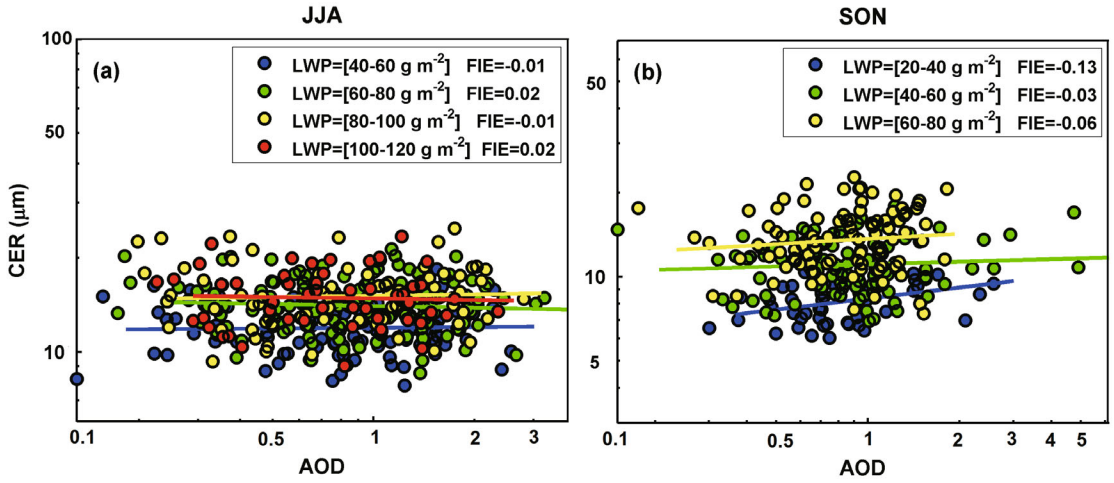

Fig. 9. CER as a function of AOD for different LWP bins: (a) JJA; (b) SON. Data are from MODIS on the Terra and Aqua platforms and cover the period 2003–12.

face measurements may be influenced more by aerosols than the CER derived from satellite measurements because there is more contact between cloud particles near the cloud base and aerosols (Liu et al., 2016). A third possible reason involves the uncertainties in AOD retrievals due to cloud contamination. A study by Várnai and Marshak (2014) revealed that satellite-retrieved AOD for roughly half of the pixels within 5 km of clouds can be up to 50% greater than the AOD for pixels further away from clouds. Thus, satellite retrievals made near clouds can lead to spurious correlations between aerosol and cloud parameters (Costantino and Bréon, 2013). Also, the AOD retrieved from MODIS measurements does not represent real aerosol loading in the atmosphere because the retrieval is enhanced by aerosol swelling effects (Jeong and Li, 2010). The relationship between AOD and CCN is significantly influenced by RH (Liu and Li, 2014).

4. Summary

The ARM mobile facility was stationed at SX in southeastern China from May to December 2008 with the purpose of collecting measurements aimed at studying the influence of aerosols on radiative fluxes, clouds, and precipitation. To the authors' knowledge, this was the first time that simultaneous measurements of cloud, aerosol, and radiative properties, as well as meteorological quantities, were made in this key region. This study presents the statistics of aerosol and cloud properties in different seasons and under different air mass conditions, then examines the influences of aerosols on cloud properties based on surface measurements made at this heavily polluted site.

In both summer and fall, CER decreases as AI increases, but the relationship is weaker in summer. There is little dependence of LWP on AI in summer, but in fall LWP increases significantly with increasing AI. There is a significant increase in COD as AI increases in fall, but not in summer. When air mass II (originating from northeastern China) and III (originating from over the ocean to the east of the site) influence the site, CER (COD) significantly decreases (increases) with increasing AI.

There is a shift in percentage changes in hourly mean CER (ΔCER) toward positive and negative values for the lowest (ΔAI_L) and highest (ΔAI_H) quartile of percentage changes in AI cases, respectively. For the ΔAI_L case, the mean ΔCER is 0.18 (an increase of 18%), and for the ΔAI_H case the mean ΔCER is -0.06 (a decrease of 6%). This suggests that, when the AI increases after an hour, the CER tends to decrease, and LWP and COD tend to increase simultaneously. The magnitude of the aerosol FIE with respect to both CER and COD in summer and fall and for air mass II and III was estimated based on ground-based measurements divided into different LWP bins. The mean FIE_{CER} in summer (fall) is equal to 0.16 ± 0.06 (0.17 ± 0.06) and equal to 0.23 ± 0.09 (0.20 ± 0.06) when air mass II (III) influences the site. The magnitudes of mean FIE_{COD} in summer and fall and for each air mass type are similar to those of FIE_{CER}. This suggests that the FIE has no systematically strong seasonal variation and no significant difference under different air mass conditions at the SX site.

Ten years (2003–2012) of MODIS/Terra and MODIS/Aqua AOD and cloud microphysical properties retrieved at the SX site were also used to estimate the FIE from a space-based perspective. The effect of aerosols on cloud microphysical properties retrieved from satellite measurements is weak, and even contrary to the Twomey effect, and is affected by much more noise. Possible reasons are discussed. Results from studies about the aerosol indirect effect based on satellite measurements are contrary to results from surface-based retrievals, and may have large uncertainties due to some inherent limitations.

The FIE estimated in our study may be influenced by interactions and feedbacks with aerosol properties (e.g., aerosol vertical distribution, aerosol size distribution, etc.) and meteorological dynamics (e.g., vertical velocity and vertical wind shear). These quantities are difficult to measure simultaneously and are not discussed here. More studies focused on aerosol–cloud interactions are still needed in China, which is

an ideal test bed for studying aerosol indirect effects due to the abundance of anthropogenic and natural aerosol particles in the atmosphere over that region.

Acknowledgements. Data were obtained from the ARM Program sponsored by the U.S. Department of Energy, Office of Science, Office of Biological and Environmental Research, Climate and Environmental Sciences Division. The reanalysis data were obtained from the ECMWF model runs for ARM analysis provided by the ECMWF. M. Cribb helped edit the manuscript. The study was supported by the National Basic Research "973" Program of China (Grant No. 2013CB955804), a Natural Science Foundation of China research project (Grant No. 91544217), and the U.S. National Science Foundation (Grant No. AGS1534670).

REFERENCES

Bréon, F.-M., D. Tanré, and S. Generosol, 2002: Aerosol effect on cloud droplet size monitored from satellite. *Science*, **295**, 834–838, https://doi.org/10.1126/science.1066434.

Bulgin, C. E., and Coauthors, 2008: Regional and seasonal variations of the Twomey indirect effect as observed by the ATSR-2 satellite instrument. *Geophys. Res. Lett.*, **35**, L02811, https://doi.org/10.1029/2007GL031394.

Chiu, J. C., C.-H. Huang, A. Marshak, I. Slutsker, D. M. Giles, B. N. Holben, Y. Knyazikhin, and W. J. Wiscombe, 2010: Cloud optical depth retrievals from the Aerosol Robotic Network (AERONET) cloud mode observations. *J. Geophys. Res.*, **115**, D14202, https://doi.org/10.1029/2009JD013121.

Chiu, J. C., and Coauthors, 2012: Cloud droplet size and liquid water path retrievals from zenith radiance measurements: Examples from the Atmospheric Radiation MEASUREMENT Program and the Aerosol Robotic Network. *Atmos. Chem. Phys.*, **12**(21), 10 313–10 329, https://doi.org/10.5194/acp-12-10313-2012.

Costantino, L., and F.-M. Bréon, 2013: Aerosol indirect effect on warm clouds over South-East Atlantic, from co-located MODIS and CALIPSO observations. *Atmos. Chem. Phys.*, **13**(1), 69–88, https://doi.org/10.5194/acp-13-69-2013.

Dong, X. Q., P. Minnis, B. K. Xi, S. Sun-Mack, and Y. Chen, 2008: Comparison of CERES-MODIS stratus cloud properties with ground-based measurements at the DOE ARM Southern Great Plains site. *J. Geophys. Res.*, **113**, D03204, https://doi.org/10.1029/2007JD008438.

Fan, J. W., L. R. Leung, Z. Q. Li, H. Morrison, H. B. Chen, Y. Q. Zhou, Y. Qian, and Y. Wang, 2012: Aerosol impacts on clouds and precipitation in eastern China: Results from bin and bulk microphysics. *J. Geophys. Res.*, **117**, D00K36, https://doi.org/10.1029/2011JD016537.

Fan, X. H., H. B. Chen, X. G. Xia, Z. Q. Li, and M. Cribb, 2010: Aerosol optical properties from the Atmospheric Radiation Measurement Mobile Facility at Shouxian, China. *J. Geophys. Res.*, **115**(D7), D00K33, https://doi.org/10.1029/2010JD014650.

Feingold, G., W. L. Eberhard, D. E. Veron, and M. Previdi, 2003: First measurements of the Twomey indirect effect using ground-based remote sensors. *Geophys. Res. Lett.*, **30**(6), https://doi.org/10.1029/2002GL016633.

Feingold, G., R. Furrer, P. Pilewskie, L. A. Remer, Q. L. Min, and H. Jonsson, 2006: Aerosol indirect effect studies at Southern Great Plains during the May 2003 Intensive Operations Period. *J. Geophys. Res.*, **111**, D05S14, https://doi.org/10.1029/2004JD005648.

Garrett, T. J., C. Zhao, X. Dong, G. G. Mace, and P. V. Hobbs, 2004: Effects of varying aerosol regimes on low-level Arctic stratus. *Geophys. Res. Lett.*, **31**, L17105, https://doi.org/10.1029/2004GL019928.

Harikishan, G., B. Padmakumari, R. S. Maheskumar, G. Pandithurai, and Q. L. Min, 2016: Aerosol indirect effects from ground-based retrievals over the rain shadow region in Indian subcontinent. *J. Geophys. Res.*, **121**, 2369–2382, https://doi.org/10.1002/2015JD024577.

Heintzenberg, J., and Coauthors, 2006: Intercomparisons and aerosol calibrations of 12 commercial integrating nephelometers of three manufacturers. *J. Atmos. Oceanic Technol.*, **23**, 902–914, https://doi.org/10.1175/jtech1892.1.

Holben, B. N., and Coauthors, 1998: AERONET-a federated instrument network and data archive for aerosol characterization. *Remote Sensing of Environment*, **66**, 1–16, https://doi.org/10.1016/S0034-4257(98)00031-5.

IPCC, 2013: Climate Change 2013: The Physical Science Basis. Contribution of Working Group I to the Fifth Assessment Report of the Intergovernmental Panel on Climate Change, T. F. Stocker, et al., Eds, Cambridge University Press, Cambridge, United Kingdom and New York, NY, USA, 1535pp, https://doi.org/10.1017/CBO9781107415324.

Jeong, M.-J., and Z. Q. Li, 2010: Separating real and apparent effects of cloud, humidity, and dynamics on aerosol optical thickness near cloud edges. *J. Geophys. Res.*, **115**, D00K32, https://doi.org/10.1029/2009JD013547.

Kim, B.-G., S. E. Schwartz, M. A. Miller, and Q. L. Min, 2003: Effective radius of cloud droplets by ground-based remote sensing: Relationship to aerosol. *J. Geophys. Res.*, **108**(D23), 4740, https://doi.org/10.1029/2003JD003721.

Kim, B.-G., M. A. Miller, S. E. Schwartz, Y. G. Liu, and Q. L. Min, 2008: The role of adiabaticity in the aerosol first indirect effect. *J. Geophys. Res.*, **113**, D05210, https://doi.org/10.1029/2007JD008961.

Lee, K. H., Z. Q. Li, M. C. Cribb, J. J. Liu, L. Wang, Y. F. Zheng, X. G. Xia, H. B. Chen, and B. Li, 2010: Aerosol optical depth measurements in eastern China and a new calibration method. *J. Geophys. Res.*, **115**, D00K11, https://doi.org/10.1029/2009JD012812.

Lee, S. S., J. E. Penner, and S. M. Saleeby, 2009: Aerosol effects on liquid-water path of thin stratocumulus clouds. *J. Geophys. Res.*, **114**, D07204, https://doi.org/10.1029/2008JD010513.

Li, Z., and Coauthors, 2009: Uncertainties in satellite remote sensing of aerosols and impact on monitoring its long-term trend: A review and perspective. *Annales Geophysicae*, **27**, 2755–2770, https://doi.org/10.5194/angeo-27-2755-2009.

Li, Z. Q., and Coauthors, 2007: Preface to special section on East Asian studies of tropospheric aerosols: An international regional experiment (EAST-AIRE). *J. Geophys. Res.*, **112**, D22S00, https://doi.org/10.1029/2007JD008853.

Li, Z. Q., and Coauthors, 2011: East Asian studies of tropospheric aerosols and their impact on regional climate (EAST-AIRC): An overview. *J. Geophys. Res.*, **116**, D00K34, https://doi.org/10.1029/2010JD015257.

Liljegren J. C., and B. M. Lesht, 2004: Preliminary results with the twelve-channel microwave radiometer profiler at the North Slope of Alaska Climate Research Facility. *Fourteenth ARM*

Science Team Meeting Proceedings, Albuquerque, New Mexico.

Liljegren, J. C., E. E. Clothiaux, G. G. Mace, S. Kato, and X. Q. Dong, 2001: A new retrieval for cloud liquid water path using a ground-based microwave radiometer and measurements of cloud temperature. *J. Geophys. Res.*, **106**, 14 485–14 500, https://doi.org/10.1029/2000JD900817.

Liu, G. S., H. F. Shao, J. A. Coakley Jr., J. A. Curry, J. A. Haggerty, and M. A. Tschudi, 2003: Retrieval of cloud droplet size from visible and microwave radiometric measurements during INDOEX: Implication to aerosols' indirect radiative effect. *J. Geophys. Res.*, **108**(D1), 4006, https://doi.org/10.1029/2001JD001395.

Liu, J. J., and Z. Q. Li, 2014: Estimation of cloud condensation nuclei concentration from aerosol optical quantities: Influential factors and uncertainties. *Atmos. Chem. Phys.*, **14**(1), 471–483, https://doi.org/10.5194/acp-14-471-2014.

Liu, J. J., Y. F. Zheng, Z. Q. Li, C. Flynn, E. J. Welton, and M. Cribb, 2011a: Transport, vertical structure and radiative properties of dust events in southeast China determined from ground and space sensors. *Atmos. Environ.*, **45**(35), 6469–6480, https://doi.org/10.1016/j.atmosenv.2011.04.031.

Liu, J. J., Y. F. Zheng, Z. Q. Li, and M. Cribb, 2011b: Analysis of cloud condensation nuclei properties at a polluted site in southeastern China during the AMF-China Campaign. *J. Geophys. Res.*, **116**, D00K35, https://doi.org/10.1029/2011JD016395.

Liu, J. J., Y. F. Zheng, Z. Q. Li, C. Flynn, and M. Cribb, 2012: Seasonal variations of aerosol optical properties, vertical distribution and associated radiative effects in the Yangtze Delta region of China. *J. Geophys. Res.*, **117**, D00K38, https://doi.org/10.1029/2011JD016490.

Liu, J. J., Z. Q. Li, Y. F. Zheng, J. C. Chiu, F. S. Zhao, M. Cadeddu, F. Z. Weng, and M. Cribb, 2013: Cloud optical and microphysical properties derived from ground-based and satellite sensors over a site in the Yangtze Delta region. *J. Geophys. Res.*, **118**, 9141–9152, https://doi.org/10.1002/jgrd.50648.

Liu, J. J., Z. Q. Li, Y. F. Zheng, and M. Cribb, 2015: Cloud-base distribution and cirrus properties based on micropulse lidar measurements at a site in southeastern China. *Adv. Atmos. Sci.*, **32**(7), 991–1004, https://doi.org/10.1007/s00376-014-4176-2.

Liu, J. J., Z. Q. Li, and M. Cribb, 2016: Response of marine boundary layer cloud properties to aerosol perturbations associated with meteorological conditions from the 19-Month AMF-Azores campaign. *J. Atmos. Sci.*, **73**(11), 4253–4268, https://doi.org/10.1175/JAS-D-15-0364.1.

Ma, J. Z., Y. Chen, W. Wang, P. Yan, H. J. Liu, S. Y. Yang, Z. J. Hu, and J. Lelieveld, 2010: Strong air pollution causes widespread haze-clouds over China. *J. Geophys. Res.*, **115**, D18204, https://doi.org/10.1029/2009JD013065.

Marshak, A., Y. Knyazikhin, K. D. Evans, and W. J. Wiscombe, 2004: The "RED versus NIR" plane to retrieve broken-cloud optical depth from ground-based measurements. *J. Atmos. Sci.*, **61**, 1911–1925, https://doi.org/10.1175/1520-0469(2004)061<1911:TRVNPT>2.0.CO;2.

McComiskey, A., and G. Feingold, 2008: Quantifying error in the radiative forcing of the first aerosol indirect effect. *Geophys. Res. Lett.*, **35**, L02810, https://doi.org/10.1029/2007GL032667.

McComiskey, A., and G. Feingold, 2012: The scale problem in quantifying aerosol indirect effects. *Atmos. Chem. Phys.*, **12**(2), 1031–1049, https://doi.org/10.5194/acp-12-1031-2012.

McComiskey, A., G. Feingold, A. S. Frisch, D. D. Turner, M. A. Miller, J. C. Chiu, Q. L. Min, and J. A. Ogren, 2009: An assessment of aerosol-cloud interactions in marine stratus clouds based on surface remote sensing. *J. Geophys. Res.*, **114**, D09203, https://doi.org/10.1029/2008JD011006.

Menon, S., A. D. Del Genio, Y. Kaufman, R. Bennartz, D. Koch, N. Loeb, and D. Orlikowski, 2008: Analyzing signatures of aerosol-cloud interactions from satellite retrievals and the GISS GCM to constrain the aerosol indirect effect. *J. Geophys. Res.*, **113**, D14S22, https://doi.org/10.1029/2007JD009442.

Min, Q.-L., M. Duan, and R. Marchand, 2003: Validation of surface retrieved cloud optical properties with in situ measurements at the Atmospheric Radiation Measurement Program (ARM) South Great Plains site. *J. Geophys. Res.*, **108**(D17), https://doi.org/10.1029/2003jd003385.

Myhre, G., and Coauthors, 2007: Aerosol-cloud interaction inferred from MODIS satellite data and global aerosol models. *Atmos. Chem. Phys.*, **7**, 3081–3101, https://doi.org/10.5194/acp-7-3081-2007.

Nakajima, T., A. Higurashi, K. Kawamoto, and J. E. Penner, 2001: A possible correlation between satellite derived cloud and aerosol microphysical parameters. *Geophys. Res. Lett.*, **28**(7), 1171–1174, https://doi.org/10.1029/2000GL012186.

Pandithurai, G., T. Takamura, J. Yamaguchi, K. Miyagi, T. Takano, Y. Ishizaka, S. Dipu, and A. Shimizu, 2009: Aerosol effect on cloud droplet size as monitored from surface-based remote sensing over East China Sea region. *Geophys. Res. Lett.*, **36**, L13805, https://doi.org/10.1029/2009GL038451.

Quaas, J., and Coauthors, 2009: Aerosol indirect effects-General circulation model intercomparison and evaluation with satellite data. *Atmos. Chem. Phys.*, **9**, 8697–8717, https://doi.org/10.5194/acp-9-8697-2009.

Rolph, G. D., 2016: Real-time Environmental Applications and Display System (READY). NOAA Air Resources Laboratory, College Park, MD.

Rosenfeld, D., and G. Feingold, 2003: Explanation of the discrepancies among satellite observations of the aerosol indirect effects. *Geophys. Res. Lett.*, **30**(14), https://doi.org/10.1029/2003GL017684.

Stein, A. F., R. Draxle, G. D. Rolph, B. J. B. Stunder, M. D. Cohen, and F. Ngan, 2015: NOAA's HYSPLIT atmospheric transport and dispersion modeling system. *Bull. Amer. Meteor. Soc.*, **96**, 2059–2077, https://doi.org/10.1175/BAMS-D-14-00110.1.

Tang, J. P., P. C. Wang, L. J. Mickley, X. G. Xia, H. Liao, X. Yue, L. Sun, and J. R. Xia, 2014: Positive relationship between liquid cloud droplet effective radius and aerosol optical depth over Eastern China from satellite data. *Atmos. Environ.*, **84**, 244–253, https://doi.org/10.1016/j.atmosenv.2013.08.024.

Twohy, C. H., M. D. Petters, J. R. Snider, B. Stevens, W. Tahnk, M. Wetzel, L. Russell, and F. Burnet, 2005: Evaluation of the aerosol indirect effect in marine stratocumulus clouds: Droplet number, size, liquid water path, and radiative impact. *J. Geophys. Res.*, **110**, D08203, https://doi.org/10.1029/2004JD005116.

Twomey, S., 1977: The influence of pollution on the shortwave albedo of clouds. *J. Atmos. Sci.*, **34**(7), 1149–1152, https://doi.org/10.1175/1520-0469(1977)034<1149:TIOPOT>2.0.CO;2.

Várnai, T., and A. Marshak, 2014: Near-cloud aerosol properties from the 1-km resolution MODIS ocean product. *J. Geophys. Res.*, **119**, 1546–1554, https://doi.org/10.1002/2013JD020633.

Wang, F., J. P. Guo, Y. R. Wu, X. Y. Zhang, M. J. Deng, X. W. Li, J. H. Zhang, and J. Zhao, 2014: Satellite observed aerosol-induced variability in warm cloud properties under different meteorological conditions over eastern China. *Atmos. Environ.*, **84**, 122–132, https://doi.org/10.1016/j.atmosenv.2013.11.018.

Wang, M. H., and Coauthors, 2012: Constraining cloud lifetime effects of aerosols using A-Train satellite observations. *Geophys. Res. Lett.*, **39**, L15709, https://doi.org/10.1029/2012GL052204.

Wang, Y., J. W. Fan, R. Y. Zhang, L. R. Leung, and C. Franklin, 2013: Improving bulk microphysics parameterizations in simulations of aerosol effects. *J. Geophys. Res.*, **118**, 5361–5379, https://doi.org/10.1002/jgrd.50432.

Wang, Z. E., and K. Sassen, 2001: Cloud type and macrophysical property retrieval using multiple remote sensors. *J. Appl. Meteor.*, **40**, 1665–1682, https://doi.org/10.1175/1520-0450(2001)040<1665:CTAMPR>2.0.CO;2.

Xia, X. G., Z. Q. Li, B. Holben, P. C. Wang, T. Eck, H. B. Chen, M. Cribb, and Y. X. Zhao, 2007: Aerosol optical properties and radiative effects in the Yangtze Delta region of China. *J. Geophys. Res.*, **112**, D22S12, https://doi.org/10.1029/2007JD008859.

Xu, J., M. H. Bergin, X. Yu, G. Liu, J. Zhao, C. M. Carrico, and K. Baumann, 2002: Measurement of aerosol chemical, physical and radiative properties in the Yangtze delta region of China. *Atmos. Environ.*, **36**(2), 161–173, https://doi.org/10.1016/S1352-2310(01)00455-1.

Yuan, T. L., Z. Q. Li, R. Y. Zhang, and J. W. Fan, 2008: Increase of cloud droplet size with aerosol optical depth: An observation and modeling study. *J. Geophys. Res.*, **113**, D04201, https://doi.org/10.1029/2007JD008632.

Zhang, S. P., and Coauthors, 2016: On the characteristics of aerosol indirect effect based on dynamic regimes in global climate models. *Atmos. Chem. Phys.*, **16**(5), 2765–2783, https://doi.org/10.5194/acp-16-2765-2016.

Zhao, C. F., S. A. Klein, S. C. Xie, X. H. Liu, J. S. Boyle, and Y. Y. Zhang, 2012: Aerosol first indirect effects on non-precipitating low-level liquid cloud properties as simulated by CAM5 at ARM sites. *Geophys. Res. Lett.*, **39**, L08806, https://doi.org/10.1029/2012GL051213.